

Tellurium-assisted growth of large-scale atom-thin insulating amorphous carbon on insulating substrates

Received: 2 June 2025

Accepted: 1 September 2025

Published online: 03 October 2025

Check for updates

Ya Deng^{1,15}, Zihao Wang^{2,15}, Zhili Hu^{3,15}, Ang Li^{4,15}, Xin Zhou^{1,2}, Zhaolong Chen^{2,5}, Xingli Wang^{6,7}, Jiawei Liu², Kongyang Yi¹, Dundong Yuan⁸, Xiaowei Wang⁹, Peikun Zhang³, Chao Zhu^{1,6}, Xiaoxu Zhao¹⁰, Wei Ma¹, Yao Wu¹, Ruihuan Duan¹, Qundong Fu^{1,6}, Jiefu Yang¹, Xiuxian Zhou¹, Mengyao Cao¹, Chao Zhu⁸, Beng Kang Tay^{6,7}, Jian Zhang¹¹, Mickael Lucien Perrin^{12,13,14}, Wu Zhou⁴✉, Zhuhua Zhang³✉, Kostya S. Novoselov²✉ & Zheng Liu^{1,6}✉

Monolayer amorphous carbon (a-C), an atom-thin two-dimensional (2D) carbon amorphous material, has attracted significant attention due to its structural and transport properties. Here, we report a chemical vapor deposition (CVD) approach for directly synthesizing monolayer a-C films on insulating substrates, achieving high control over their size, thickness, and fabrication. The synthesized films exhibit a complete coverage over a 2-inch wafer, with high uniformity. Our theoretical analysis reveals the critical role of tellurium in promoting the growth of monolayer a-C on the substrate. Moreover, quantum tunneling measurements at liquid helium temperature were conducted on the a-C films, confirming the samples' homogeneity and their insulating behavior. This work provides a promising strategy for direct synthesis of atom-thin insulating amorphous materials and deepens our understanding of quantum phenomena and electronic properties in low-dimensional disordered materials.

Monolayer a-C is a one-atom-thick amorphous material comprising two-dimensional (2D), randomly interconnected networks of carbon atoms. These 2D a-C films have recently garnered substantial attention owing to their atomically thin thickness, non-crystalline nature, and potential applications^{1–5}. Since the first synthesis of monolayer a-C in 2020², current research primarily focuses on manipulating disorder structures and understanding the fundamental electrical conductivity of 2D a-C³. However, previous synthesis methods for a-C films required the use of copper substrates^{2,3}, followed by the transfer step through a chemical etching process. This method could potentially lead to residual contaminant issues and unavoidably influence fundamental studies and commercial applications of a-C films.

Apart from the growth of 2D a-C that needs improvement, a deeper understanding of its insulating behavior is equally crucial.

Previous reports primarily relied on high resistivity values around room temperatures as the main evidence to describe its transport properties and demonstrate its insulating behavior², which is not strict enough in physics as the high temperature will obscure the intrinsic properties of the material by the increased electron hopping due to the high disorder and increased thermally activated transport. In comparison, low-temperature measurements not only reduce thermal excitation, but also enable the analysis of phenomena pertaining to quantum effects. This forms the basis for utilizing quantum tunneling to investigate insulating behavior in this experiment. Moreover, the amorphous nature, featured by the absence of long-range ordering, is also explorable at low temperatures. Thus, low-temperature measurements are generally indispensable at such conditions but challenging due to the poor in-plane electrical conductivity of a-C at low

temperatures. Instead, capitalizing on the two-dimensional nature of a-C materials, quantum tunneling characterization undeniably presents a feasible option for studying electrical behavior of 2D materials at liquid helium temperature.

Herein, we present an efficient and flexible CVD method for the direct synthesis of wafer-size a-C monolayers with precise control over size and morphology on diverse substrates, thereby enabling seamless integration into standard fabrication processes. Furthermore, we investigate the low-temperature electrical properties of a-C using a unique quantum tunneling device. Our findings reveal that amorphous carbon films exhibit insulating behavior, shedding light on the

understanding of amorphous insulator and showcasing the potential for developing a-C film-based devices.

Results

Synthesis and characterization of 2D a-C

The process of synthesizing monolayer a-C film using a carbon-doped molybdenum (C-Mo) film is illustrated schematically in Fig. 1a–b. First, a C-Mo film with a thickness of ~2 nm was deposited on the Si/SiO₂ wafer via magnetron sputtering, serving as the precursor (see Supplementary Figs. 1–3, for additional details), as indicated in Fig. 1a. Then, the C-Mo film is heated in a CVD furnace (Supplementary Fig. 4).

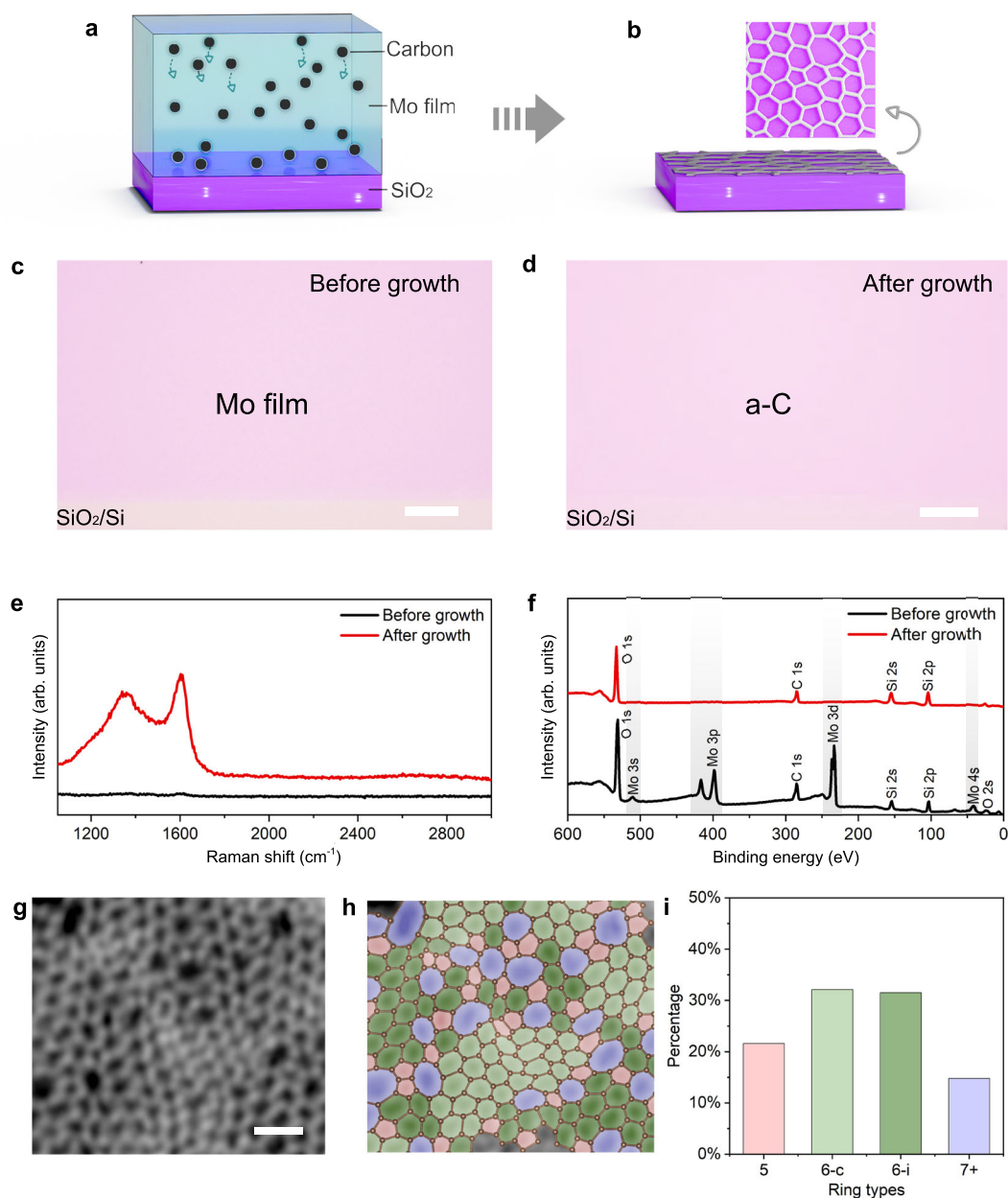


Fig. 1 | Direct growth and atomic structure of monolayer amorphous carbon (a-C) on the SiO₂/Si substrate. a, b Schematic diagrams for the 2D a-C synthesis using C-doped Mo films. **c, d** Optical images of Mo films before (c) and after synthesis (d) at 650 °C for 1 h. **e, f** Typical Raman (e) and X-ray photoelectron spectroscopy (XPS) (f) spectra of Mo film (black) and synthesized a-C (red). **g, h** Representative denoised annular dark-field scanning transmission electron microscopy (ADF-

STEM) image and the corresponding color overlays of monolayer a-C. Each color corresponds to a specific type of carbon ring: pink for five-membered rings (5), green for six-membered rings (crystallite regions in light green (6-c) and isolated hexagonal regions in dark green (6-i)), and purple for rings containing seven or more carbon atoms (7+). **i** Statistics of different types of carbon rings in (h). Scale bars: 20 μm in (c, d), 0.5 nm in (g).

During this process, the molybdenum evaporates, and carbon atoms coalesce to form an a-C film, progressing from stage I (Fig. 1a) to stage II (Fig. 1b). The experimental procedure can be found in the “Methods” section, along with detailed information provided in Supplementary Figs. 5–9.

Optical images of the ultra-thin C-Mo precursor film and the synthesized 2D a-C film are presented in Fig. 1c and d, respectively, both exhibiting a uniform and continuous appearance. However, the difference between the two films is discernable in the Raman spectrum and X-ray photoelectron spectroscopy (XPS) data (Fig. 1e, f). Notably, prior to growth, no Raman peaks pertaining to carbon are observed. Following the growth process, distinct Raman D and G bands, characteristic features of graphitic materials⁶, become prominent. These findings suggest the formation of carbon bonding during the growth process. Importantly, the broadened nature of the Raman D and G peaks results in a slight overlap with each other, which, together with the absence of the 2D peak, signifies a lack of long-range order in the lattice^{7–9}. This observation aligns with the characteristic features of previously reported a-C materials^{2,3}. XPS analysis was employed to monitor the compositional changes of the precursor film, showing no detectable Mo signal after the growth process (Fig. 1f and Supplementary Fig. 10). This result was further validated by transmission electron microscopy (TEM) and energy-dispersive X-ray spectroscopy (EDX) characterizations (Supplementary Figs. 11 and 12). Furthermore, the Raman maps and SEM images shown in Supplementary Figs. 13 and 14 confirm the uniform nature of the synthesized a-C films. Next, annular dark-field scanning transmission electron microscopy (ADF-STEM) analysis was conducted to confirm the amorphous nature of the carbon film at atomic scale. The representative STEM image in Fig. 1g shows a typical monolayer amorphous carbon structure, characterized by a contiguous network of carbon atoms reminiscent of graphene but lacking long-range periodic order. Then, the color-coding overlays illustrated in Fig. 1h highlights the structural distinctions between the a-C and conventional graphene. Compared with uniform hexagonal rings formed by sp^2 -hybridized carbon atoms in graphene, the rings in the a-C may consist of 5 to 9 atoms with a non-uniform distribution. Pink represents five-membered rings, green represents six-membered rings, and purple represents rings containing seven or more carbon atoms. The six-membered carbon rings are further subdivided into crystallite regions indicated in light green, and isolated regions indicated in dark green, following the method reported previously³, where the crystallites are defined as regions comprising at least a central hexagon with six adjacent hexagonal rings. The statistics for the different types of carbon rings in Fig. 1i show ratios consistent with those previously reported for the monolayer a-C material³. More statistical analyses based on the STEM images further substantiate the absence of long-range periodicity (Supplementary Fig. 15). Finally, the TEM/STEM images acquired from multiple locations (Supplementary Figs. 16 and 17) and selected-area electron diffraction (SAED) patterns obtained from micron-scale regions further confirm the amorphous nature of the a-C films (Supplementary Fig. 18).

Figure 2 shows the wafer-size 2D a-C films, high-resolution sample patterning, and substrate engineering. Figure 2a showcases 2-inch a-C films on SiO_2/Si wafer, underscoring the capability of our method in fabricating a-C films of arbitrary sizes. Raman analysis reveals the uniformity of the a-C film, as evidenced by consistent Raman D and G peaks throughout the film-covered area (Supplementary Fig. 19). Furthermore, Raman G peak intensity mapping collected at multiple positions across the a-C wafer further supports this homogeneity (Fig. 2b). Additionally, our method allows for the pre-patterning of the C-Mo precursor, facilitating the direct growth of a-C into a pre-determined geometry with good uniformity (Fig. 2c–f, and Supplementary Fig. 20). This morphology-controllable synthesis, previously unattainable with copper substrate-based methods, broadens the

scope of applications for amorphous materials. Furthermore, a-C can be grown on diverse substrates, as illustrated by the uniform samples on sapphire and quartz substrates (Supplementary Fig. 21). Moreover, we can also obtain a-C films with controlled thickness (Supplementary Fig. 22) equivalent to monolayer to trilayer. These results highlight the versatility of our method, including the direct synthesis of a-C on insulating substrates, establishing a robust platform for exploring wafer-scale synthesis strategies. They also underscore the potential of amorphous materials for scalable production, customizable patterning, and compatibility with diverse substrates.

Formation mechanism of 2D a-C

Controlled experiments, simulation and theory calculations have been performed to understand the formation mechanism of 2D a-C. Our experiments (Supplementary Figs. 5–7) show that the supply of a trace amount of tellurium (Te) source during the growth is key to facilitate the formation of 2D a-C film (Fig. 3a). To elucidate the role of Te atoms, kinetic Monte Carlo (kMC) simulations of the growth process were conducted. Given that the research on monolayer a-C system is still in its early stages and lacks qualitative understanding^{2,3,10}, a coarse-grain kMC model based on energy-driven kMC (EDKMC)^{11–14} was developed to understand the experimental results qualitatively. Density function theory (DFT) calculations were also employed to evaluate carbon-substrate interactions, subsequently used as an input of van der Waals (vdW) parameters in kMC simulations (Fig. 3d). More details can be found in the “Methods” section and Supplementary Fig. 23. Simulations indicate that a minute a-C sheet emerges from the nucleus on an amorphous SiO_2 covered substrate during growth, featuring a lattice composed of hexagons randomly mixed with pentagons, heptagons, and octagons. Yet, compared to planar graphene lattices, the presence of non-hexagon rings induces off-plane buckling¹⁵, particularly pronounced on the weakly interacting SiO_2 substrate. This off-plane buckling can accumulate during growth, biasing the growth of the carbon sheet into a 3D amorphous structure (Fig. 3b) that agrees with experimental observations (inset of Fig. 3d and Supplementary Fig. 5).

In reality, the growth front of carbon film must contain carbon radicals with dangling bonds for the growth to proceed. DFT calculations show that a free Te atom could bond between an oxygen atom of the substrate and a carbon radical at the rim of a carbon film (Fig. 3a, d). Such bridge bonding significantly strengthens the interaction between the carbon film and the substrate, particularly along the film’s rim. Incorporating this effect into our kMC simulations leads to an effective suppression of the off-plane buckling of carbon sheets, ultimately yielding a nearly flat 2D a-C film (Fig. 3c) that echoes our experimental results.

Note that the relatively flexible Te bonds at the growth temperature T_g is crucial for the growth of 2D a-C, as the breaking of a part of these unstable bonds is necessary to maintain the growth. Without this feature, Te atoms would either be consumed by covalently bridging the carbon film and substrate or terminate the growth by bonding to all carbon radicals at the growth front. Furthermore, the influence of T_g on growth was investigated. Despite the intrinsic randomness of the kMC method, the simulations suggested a trend that carbon film crystallinity is enhanced with increasing T_g , reaching a higher crystallinity at $T_g = 900^\circ\text{C}$ (Fig. 3e and Supplementary Fig. 24), which is consistent with the STEM and Raman results that observed nanographene features at 850°C (Supplementary Figs. 8 and 25). Theoretical analysis reveals that a reduced temperature favors the formation of amorphous carbon, and the Te atoms further promote the transformation of a-C into 2D sheets.

Low-temperature quantum tunneling measurements

Then, the in-plane measurements conducted on a-C films revealed a high electrical resistance, as shown in Supplementary Fig. 26, consistent with the insulating behavior reported in previous studies^{2,3}.

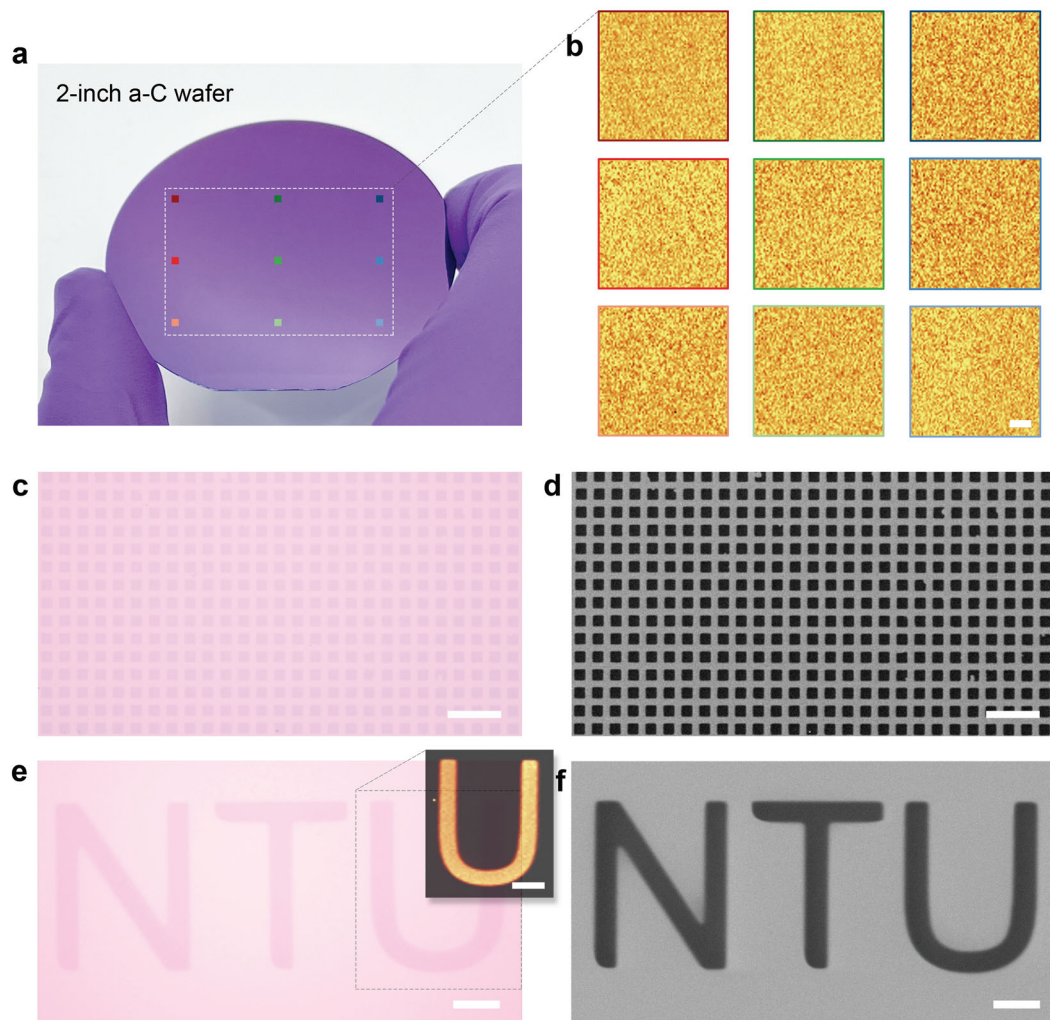


Fig. 2 | Controllable synthesis of a-C films. **a** Optical image of the synthesized 2-inch a-C wafer. **b** Raman G peak intensity mapping collected at multiple positions across a-C wafer, marked by the corresponding colored squares in white rectangular area of **(a)**, demonstrating the uniform quality of the synthesized a-C film.

c–f Optical images **(c, e)**, scanning electron microscopy (SEM) images **(d, f)** and corresponding zoomed-in Raman G peak map (inset in **e**) of the synthesized a-C patterns. Scale bars: 10 μm in **(b, e, f)**, 50 μm in **(c, d)**.

However, since these measurements were performed at high temperatures on the highly disordered carbon materials, charge transport is expected to occur via temperature-activated electron hopping. So, the data collected essentially reflects the transport mechanism of electron hopping. Notably, even for graphene, in-plane measurements can display similarly high resistance dominated by electron hopping when excessive cracks or holes are introduced during the transfer process. Therefore, more direct and effective methods are required to elucidate the origin of the insulating behavior and its relation to the amorphous nature. Thus, low-temperature electrical measurements are required to gain insights into the insulating behavior and other physical properties of the synthesized 2D a-C film. Previous studies encountered challenges due to excessive resistance, limiting measurements to near or above room temperature^{2,3}. In this study, employing an innovative architecture to measure out-of-plane tunneling properties allowed for exploring quantum-scale characteristics at liquid helium temperatures. The device architecture involved a tunneling field-effect transistor with a-C serving as a thin insulating barrier. Its detailed vertical structure is shown in Fig. 4a. Multiple tunneling junctions were fabricated on the same piece of a-C, enabling the comparison of tunneling behavior across different areas for inhomogeneity evaluation. The gold electrodes were employed as the top

electrodes, ensuring stability and a consistent Fermi level. The graphene electrode ensures that the bottom gate can adjust the position of the electrode Fermi level, thereby enabling the characterization of a broader range of transport properties. Out-of-plane measurements were conducted between a top gold electrode and its vertically corresponding bottom graphene electrode.

The I - V characteristics curves were measured at 1.6 K unless specified otherwise. The principle of I - V relation is generally described by

$$I(V_b) \propto \int dE_F \text{DoS}_B(E_F) \text{DoS}_T(E_F + eV_b) T(E_F) [f(E_F - eV_b) - f(E_F)]$$

where $\text{DoS}_B(E_F)$ and $\text{DoS}_T(E_F + eV_b)$ denote the density of states for the bottom and top electrodes, respectively. V_b is the tunneling bias shown in Fig. 4a. $T(E_F)$ represents the transmission rate through the tunneling barrier which is influenced by the barrier's bandgap. $f(E_F)$ is the Fermi-Dirac distribution, with an exponential dependence on the temperature¹⁶.

As shown in Fig. 4c, the $I - V_b$ curves of all our devices are linear around zero bias and the linear region reveals high resistivity across three tunneling junctions, confirming the reproducible insulating

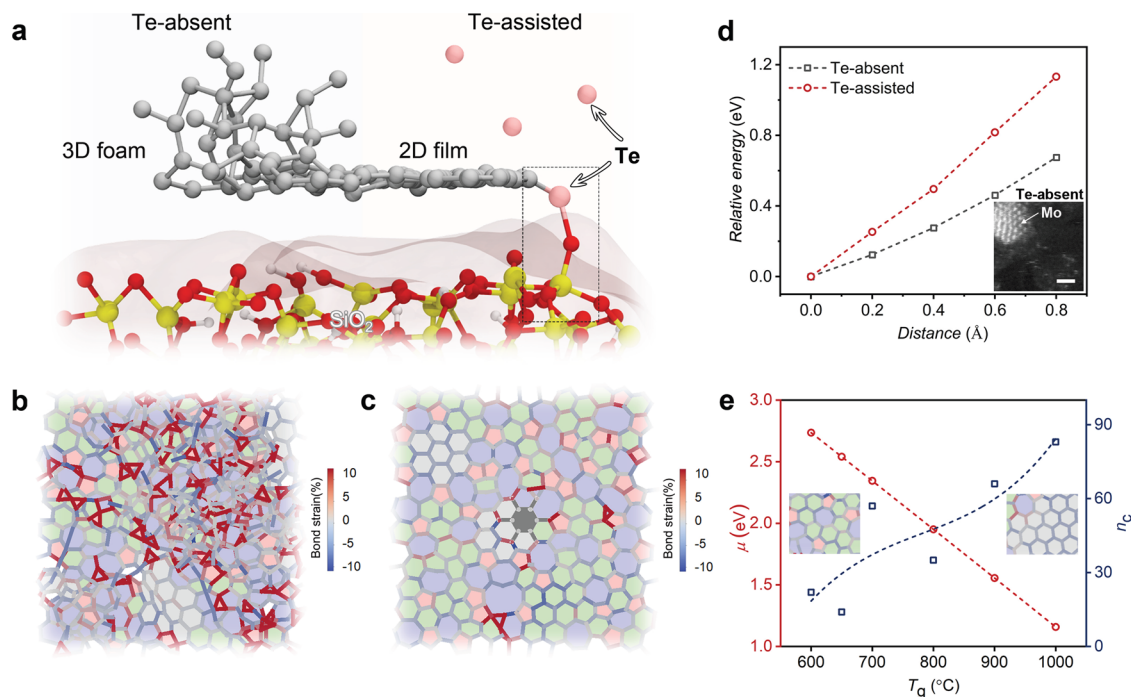


Fig. 3 | Theoretical analysis of Te-assisted synthesis of monolayer a-C film.

a Schematic of the a-C morphology and the role of Te. The black rectangle indicates the atomic structure of the contact interface for density function theory (DFT) calculations, where atoms of C, Si, O, and Te are colored gray, yellow, red, and pink, respectively. **b, c** Simulated structures representing two typical growth modes on amorphous SiO₂ substrate surfaces: a-C foam grown at $T_g = 650$ °C without Te in **(b)** and 2D a-C film grown at $T_g = 650$ °C with Te assisted in **(c)**. The number of atoms in each red, green, and purple ring is less than, equal to, and

larger than 6, respectively. Gray denotes crystalline hexagonal rings. Red and blue colors denote tensile and compressive strains in bonds, respectively. **d** Relative energies E_r vs. distance d_r obtained from DFT calculations. Inset is the STEM image of sample grown in a Te-absent atmosphere. **e** The dependence of chemical potential μ (red) and crystallinity n_c (blue) on growth temperature T_g . n_c denotes the number of crystalline hexagonal rings colored gray in Supplementary Fig. 24. The dashed red and blue curves are guides to the eye. Insets are parts of simulated a-C films grown at 600 °C and 900 °C, respectively. Scale bars: 1 nm in inset of **(d)**.

behaviors of our a-C film on a μm scale, which addresses the limitations of STEM characterization, as it is confined to evaluating material homogeneity and reliability at the local nm scale. Next, we inspect the entire profile of the I - V curve. Aside from the linear behavior at small bias, it exhibits an exponential dependence behavior at higher biases (Fig. 4d). This behavior, transitioning from linear to exponential with increasing bias, is similar to that observed in crystalline insulators like hexagonal boron nitride (hBN)¹⁶, as shown in Fig. 4d. The presence of an exponential dependence at high bias, suggests high on-off ratio like that of hBN tunneling transistors, thus offering potential applications in certain types of logic circuits. The bottom gate V_g introduces an additional degree of freedom to adjust the on-off ratio, which can modulate the extent of the linear region as illustrated in the V_b - V_g mapping (Fig. 4f). Meanwhile, we can observe some peaks in the dI_b/dV_b curve, as indicated by the blue and gray arrows. These peaks correspond to the X-shaped features marked by the same-colored arrows/dashed lines in the V_b - V_g mapping of Fig. 4f, which are attributed to defect states at the SiO₂/graphene or graphene/a-C interface^{17,18}. This observation is a result of the tunability of the bottom gate. Interestingly, the vertical stripes, observed in ordered crystal tunneling barriers of hBN and regarded as an indication of phonon-assisted tunneling¹⁷⁻¹⁹ (Fig. 4g), were not observable in a-C devices. This might further prove the absence of long-range ordering and thus support our claim of the amorphous nature of a-C¹⁹. These electrical measurements result at low temperatures where quantum effects dominate, provide robust evidence and valuable insights into such amorphous insulating materials.

In addition, we further investigated the temperature-dependent behavior of the vertical tunneling device. The evolution of I_b - V_b shape with respect to temperature is predominantly governed by the Fermi-distribution function $f(E_F)$. As temperature increases, the exponential

region diminishes, progressively giving way to the linear region (Fig. 4e), a behavior analogous to that observed in hBN. However, in contrast to insulating crystalline hBN, our theoretical calculations suggest that a-C may not possess a well-defined band gap as influenced by the amorphous nature of the atomic arrangement (Supplementary Figs. 27 and 28). Meanwhile, the average optical bandgap estimated using the Tauc method is 2.3 eV, which is generally consistent with previous reports (Supplementary Fig. 29)².

Discussion

In summary, we have successfully achieved the direct synthesis of monolayer a-C on wafer-scale substrates, offering precise control over its size, thickness, and pattern. The experiments and theoretical analyses reveal a Te-assisted growth mechanism of monolayer 2D a-C films. Moreover, the quantum tunneling characterization conducted on a-C films confirmed their homogeneity and intrinsic insulating behavior. Our results provide a flexible CVD method to directly synthesize wafer-size a-C patterns on diverse substrates. Our quantum tunneling device for investigating amorphous carbon also provides a protocol for studying insulating amorphous materials.

Methods

Deposition of precursor C-Mo film

Magnetron sputtering was used to deposit the precursor C-Mo film. An initial pre-sputtering step was performed using a carbon target to ensure the carbon content within the chamber and effectively establish a consistent carbon background. Then, switched to the Mo target and proceeded to sputter a 2 nm layer of molybdenum onto the substrate, resulting in a carbon-doped Mo film deposition. It is important to note that the carbon film was not sputtered directly, as the growth process necessitates the assistance of Mo to obtain a uniform

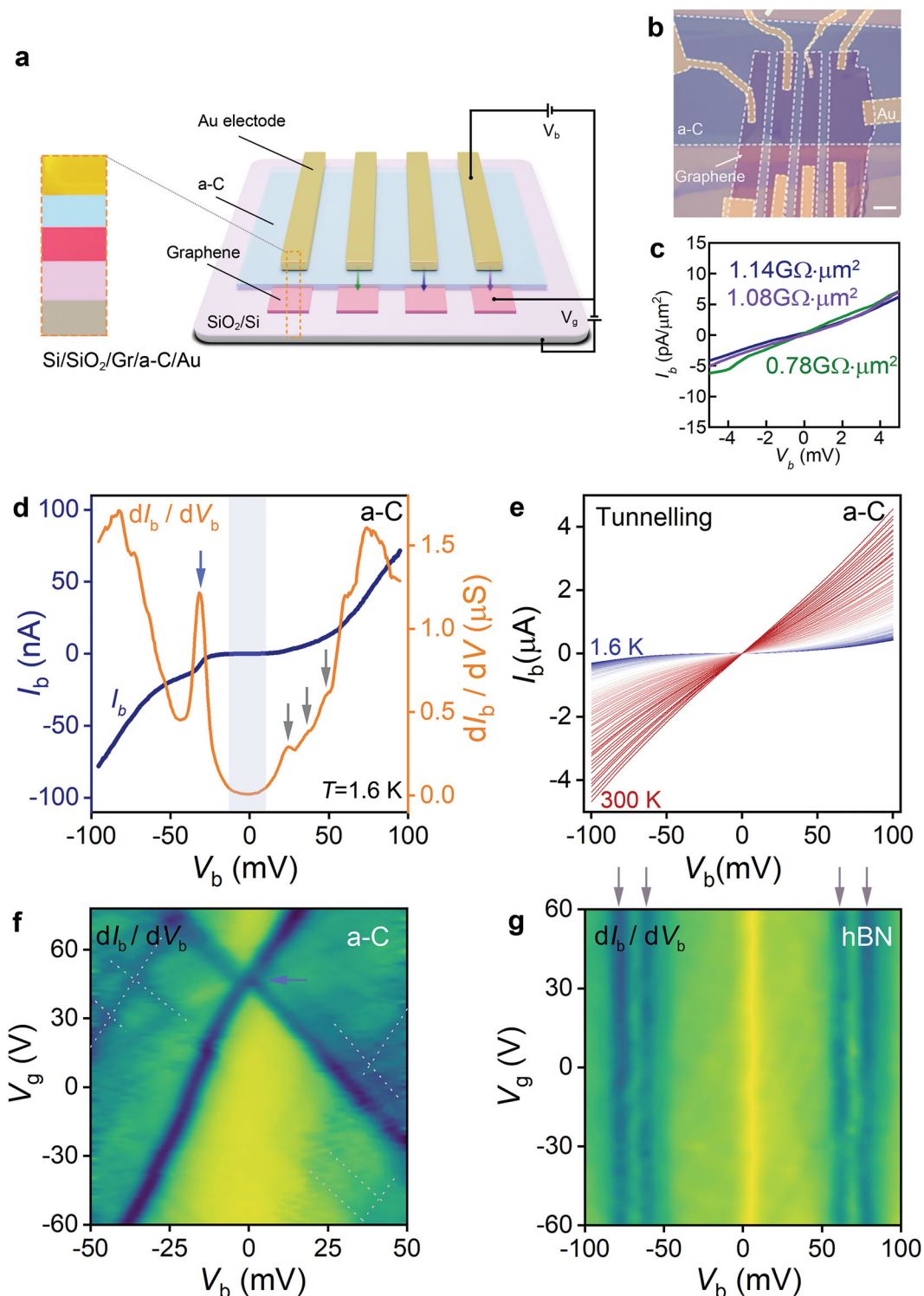


Fig. 4 | Tunneling characteristics for the Au/a-C/graphene transistor.

a Schematic structure of our tunneling device. **b** Optical image of the experimental device. The dashed line outlines the boundary of each structure. **c** The tunneling resistance close to the zero-bias region across different flake areas indicated by corresponding-colored arrows in (a). Around the zero-bias, the I_b - V_b relation is linear. Their similarities attest to the homogeneity across different regions of the sample. **d** Tunneling current (I_b) and differential conductance dI_b/dV_b as a function of source-drain bias at $V_g = -40$ V, $T = 1.6$ K. **e** The temperature evolution of I_b - V_b of

the vertical tunneling measurement. **f** The dI_b/dV_b map as a function of V_b and V_g at 1.6 K. The blue arrow and gray dashed lines indicate the defect state, corresponding to the same-colored arrow in (d). **g** The dI_b/dV_b map of comparative hBN tunneling device at 1.6 K. The gray arrows indicate the vertical feature from phonon-assisted tunneling, which is unaffected by the gate and thus appears vertical. The tunneling current, bias voltage, and bottom gate voltage are denoted as I_b , V_b , and V_g , respectively. Scale bar: 5 μm in (b).

monolayer amorphous carbon structure. Other evaporation methods, such as electron beam evaporation, are also possible, and the core is to perform coating in a carbon-containing chamber.

Synthesis of a-C film

First, the precursor C-Mo film covered sample was placed in a one-side closed quartz boat at the central heating zone of the CVD furnace (Supplementary Fig. 4). Meanwhile, the tellurium (Te) particle (50 mg) and molecular sieves (4 Å, 350 mg) were located at the closed side of the quartz boat (about 5 cm away from the sample) to serve as the precursor for the subsequent reaction. The molecular sieves were used to absorb and trap the Te atoms, ensuring that only trace amounts of the Te atoms were involved in the reaction. The concentration-controlled Te source played a pivotal role in removing molybdenum and forming the a-C film while avoiding direct reaction with the Mo film and the formation of molybdenum telluride. (Supplementary Figs. 5–7). Note that the CVD tube environment needed to be thoroughly evacuated to ensure the absence of excess oxygen residue, as the carbon is sensitive to oxygen and easy to oxidize during the heating process. Therefore, the reaction chamber was evacuated to a base pressure of 1 Torr and held for 30 min, followed by introducing argon gas to the reaction chamber until reaching atmospheric pressure. Repeat this evacuate/purge cycle three times before growth to minimize the presence of oxygen within the chamber (below 1000 ppm) and ensure a more controlled growth environment. For growth, the reaction is carried out at atmospheric pressure. The synthesis of a-C is also sensitive to the growth temperature (Supplementary Fig. 8). The furnace was heated to an optimized growth temperature (T_g) of 650 °C in 30 min and kept at this temperature for 1 h with the mixed gas of H₂/Ar with 10 and 70 sccm as the carrier gas. After growth, the furnace was naturally cooled down to room temperature.

AFM, XPS, SEM, and Raman characterization

AFM analysis was performed using the Asylum Research Cypher AFM in tapping mode. The XPS spectra were measured by the Kratos AXIS Supra spectrometer with a dual anode Al-K α (1486.6 eV) X-ray monochromatic source. SEM analysis was performed using the FESEM JEOL JSM-7600F field emission scanning electron microscope. Raman measurements were performed by WITec alpha 200R Confocal Raman system with a 532 nm excitation laser. To avoid samples overheating, the adopted laser powers were kept below 1 mW. The time-dependent Raman study of a-C was shown in Supplementary Fig. 9, to evaluate the material stability under 1 mW laser irradiation.

STEM and SAED characterization

The STEM samples were prepared by wet-etching method. The poly methyl methacrylate (PMMA) was spin-coated on the a-C film covered SiO₂/Si substrate. Then, the samples were immersed in the NaOH solution (1 M) to etch the SiO₂ layers and rinsed with DI water sequentially to remove any NaOH residue. Afterward, the PMMA-coated a-C film was carefully transferred to a Protochips heating E-chip or Quantifoil Au grid and baked at 80 °C to ensure better contact. Finally, to remove the PMMA, the sample was submerged in acetone and subsequently baked under vacuum at 250 °C for 60 min. Note that this process may lead to film rupture and should be performed with caution. The STEM characterization was conducted using JEOL ARM200F equipped with the CEOS aberration corrector, operating at 80 kV. Experiments were carried out with the Protochips Aduro heating holder at 300 °C. TEM and SAED analysis were performed using JEOL 2200FS. In an alternative heating process, a-C samples were annealed in a quartz tube under vacuum of about 10⁻⁵ mbar at 650 °C for 2 h and then cooled to room temperature. Further STEM characterization was conducted using a Nion U-HERMES100 microscope under an acceleration voltage of 60 kV (Supplementary Fig. 25), and

further EDS characterization was conducted using a JEOL GRAND-ARM2 microscope under an acceleration voltage of 80 kV (Supplementary Fig. 11). Raw ADF-STEM images were denoised using a double-Gaussian filter.

Device fabrication and electrical measurement

First, a graphene (Gr) flake was exfoliated onto a Si/SiO₂ (285 nm) substrate. Subsequently, the exfoliated Gr was selectively etched into separated ribbons to serve as the bottom electrode, employing a standard EBL-RIE method with a PMMA layer as etch resistant mask. Then the more robust trilayer a-C ribbon grown at 650 °C was selected to be transferred onto the Gr using a PPC-assisted method. Following each transfer process, the structure underwent annealing at -400 °C in an Ar/H₂ atmosphere to eliminate any residual contaminants and ensure a clean surface. Finally, the Ti/Au (5/70 nm) electrodes were fabricated to independently contact with graphene and a-C using a standard e-beam lithography (EBL) process followed by electron-beam evaporation and lift-off process. Low-temperature transport experiments were carried out in a top-loading Helium-4 refrigerator. Triax cables, the triax connector and Second Order Low Pass Filter were used to conduct signals with the highest sensitivity. The Sourcemeter 2636B was utilized to test the DC current, while the lock-in SR830 was applied for the AC measurement.

Kinetic Monte Carlo (kMC) algorithm

All simulations were carried out with a periodic boundary condition along the *xy*-direction, with neighboring periodic images separated by a vacuum space along the *z*-direction. In each simulation, the growth starts from a 12-atom nucleus, as colored gray in Fig. 3b, c. For simplicity, the unit cell is always 30 Å × 30 Å along the *xy*-directions, which corresponds to a uniform nuclei density. Equation (1) in Supplementary Note 1 is used to describe the interaction between carbon atoms and the substrate. To interpret the DFT results into parameters that can be used in kMC simulations, we fit Supplementary Equation (1) with the results presented in Fig. 3b. Then, parameters are obtained as $\tilde{\sigma} = 3.4$ Å, $\tilde{\epsilon} = 0.08$ eV for carbon radicals (i.e., carbon atoms with less than 3 C-C bonds/atom) under the Te atmosphere, and a much weaker interaction of $\tilde{\sigma} = 3.4$ Å, $\tilde{\epsilon} = 0.0045$ eV for any other carbon atoms, presuming that $\rho = 1.9 \times 10^{19}$ m⁻². A series of growth temperatures of $T_g \in [600, 1000]$ °C were tested. We have also considered the change of chemical potentials of carbon feedstock associated with T_g (Fig. 3c and Supplementary Fig. 24). More calculation details are shown in Supplementary Note 1.

DFT calculations

The DFT calculations were implemented by using Vienna *ab-initio* simulation package (VASP)^{20–22}. The Perdew-Burke-Ernzerhof (PBE) with generalized gradient approximation (GGA) was employed for the exchange-correlation function²³. A plane wave basis with a cutoff energy of 400 eV was chosen in this work. A 3 × 3 × 1 *k*-point mesh was used in these calculations. We considered the vdW interaction using the DFT-D3 method²⁴. Meanwhile, the dipole correction to the total energy was adopted. A vacuum layer along the out-plane direction of 15 Å was constructed to restrain the interactions between adjacent slabs. The residual force and energy convergence thresholds were set to 0.05 eV Å⁻¹ and 10⁻⁴ eV Å⁻¹, respectively. The structure of amorphous SiO₂ (Supplementary Fig. 23) is obtained by REAXFF molecular dynamics at 2500 K and then optimized. The total energy E_t was recorded as a function of the relative distance $d_r = d - d_0$, where d is the distance between the carbon film and the substrate, while d_0 is the d at which E_t is minimal. The relative energy $E_r = E_t - E_{t0}$ is plotted in Fig. 3d, where E_{t0} is the minimal E_t . Noticeably, the Te–O bond energy from our calculation is 0.99 eV, and the Te–C bond energy is known as 1.12 eV²⁵. These low bond energies indicate Te– bonds are unstable under the growth temperature and can break from time to time.

Reporting summary

Further information on research design is available in the Nature Portfolio Reporting Summary linked to this article.

Data availability

The Source data underlying the figures of this study are available with the paper. All raw data generated during the current study are available from the corresponding authors upon request. Source data are provided with this paper.

References

- Joo, W.-J. et al. Realization of continuous Zachariasen carbon monolayer. *Sci. Adv.* **3**, e1601821 (2017).
- Toh, C.-T. et al. Synthesis and properties of free-standing monolayer amorphous carbon. *Nature* **577**, 199–203 (2020).
- Tian, H. et al. Disorder-tuned conductivity in amorphous monolayer carbon. *Nature* **615**, 56–61 (2023).
- Felix, L. C., Tromer, R. M., Autreto, P. A. S., Ribeiro Junior, L. A. & Galvao, D. S. On the mechanical properties and thermal stability of a recently synthesized monolayer amorphous carbon. *J. Phys. Chem. C* **124**, 14855–14860 (2020).
- Bai, X. et al. Nitrogen-doped amorphous monolayer carbon. *Nature* **634**, 80–84 (2024).
- Malard, L. M., Pimenta, M. A., Dresselhaus, G. & Dresselhaus, M. S. Raman spectroscopy in graphene. *Phys. Rep.* **473**, 51–87 (2009).
- Zhao, T. et al. Ultrafast growth of nanocrystalline graphene films by quenching and grain-size-dependent strength and bandgap opening. *Nat. Commun.* **10**, 4854 (2019).
- Cançado, L. G. et al. Quantifying defects in graphene via raman spectroscopy at different excitation energies. *Nano Lett.* **11**, 3190–3196 (2011).
- Zandiatashbar, A. et al. Effect of defects on the intrinsic strength and stiffness of graphene. *Nat. Commun.* **5**, 3186 (2014).
- Zhang, Y.-T. et al. Structure of amorphous two-dimensional materials: elemental monolayer amorphous carbon versus binary monolayer amorphous boron nitride. *Nano Lett.* **22**, 8018–8024 (2022).
- Ding, F. & Yakobson, B. I. Energy-driven kinetic Monte Carlo method and its application in fullerene coalescence. *J. Phys. Chem. B* **5**, 2922–2926 (2014).
- Xu, Z., Yan, T. & Ding, F. Atomistic simulation of the growth of defect-free carbon nanotubes. *Chem. Sci.* **6**, 4704–4711 (2015).
- Hu, Z., Xue, M., Zhang, Z., Guo, W. & Yakobson, B. I. Growth instability of 2D materials on non-Euclidean surfaces. *ACS Nano* **17**, 12216–12224 (2023).
- Hu, Z., Zhang, P., Guo, W., Zhang, Z. & Yakobson, B. I. Stress-dominated growth of two-dimensional materials on nonplanar substrates. *J. Mech. Phys. Solids* **157**, 104645 (2021).
- Liu, Y. Y. & Yakobson, B. I. Cones, pringles, and grain boundary landscapes in graphene topology. *Nano Lett.* **10**, 2178–2183 (2010).
- Britnell, L. et al. Field-effect tunneling transistor based on vertical graphene heterostructures. *Science* **335**, 947–950 (2012).
- Chandni, U., Watanabe, K., Taniguchi, T. & Eisenstein, J. P. Signatures of phonon and defect-assisted tunneling in planar metal–hexagonal boron nitride–graphene junctions. *Nano Lett.* **16**, 7982–7987 (2016).
- Chandni, U., Watanabe, K., Taniguchi, T. & Eisenstein, J. P. Evidence for defect-mediated tunneling in hexagonal boron nitride-based junctions. *Nano Lett.* **15**, 7329–7333 (2015).
- Vdovin, E. E. et al. Phonon-assisted resonant tunneling of electrons in graphene-boron nitride transistors. *Phys. Rev. Lett.* **116**, 186603 (2016).
- Kresse, G. & Hafner, J. Ab initio molecular-dynamics simulation of the liquid-metal-amorphous-semiconductor transition in germanium. *Phys. Rev. B* **49**, 14251–14269 (1994).

- Kresse, G. & Furthmüller, J. Efficiency of ab-initio total energy calculations for metals and semiconductors using a plane-wave basis set. *Comp. Mater. Sci.* **6**, 15–50 (1996).
- Kresse, G. & Hafner, J. Ab initio molecular dynamics for liquid metals. *Phys. Rev. B* **47**, 558–561 (1993).
- Perdew, J. P., Burke, K. & Ernzerhof, M. Generalized gradient approximation made simple. *Phys. Rev. Lett.* **77**, 3865–3868 (1996).
- Grimme, S., Antony, J., Ehrlich, S. & Krieg, H. A consistent and accurate ab initio parametrization of density functional dispersion correction (DFT-D) for the 94 elements H-Pu. *J. Chem. Phys.* **132**, 154104 (2010).
- Liao, Y. Practical electron microscopy and database. *An Online Book* (2006).

Acknowledgements

X.X.Z.¹⁰ acknowledges support from National Key R&D Program of China (2024YFE0109200), Beijing Natural Science Foundation (JQ24010, Z220020), and National Natural Science Foundation of China (52273279). Z.L. acknowledges support from Singapore National Research Foundation (NRF-CRP22-2019-0007), Singapore Ministry of Education (MOE Tier 2 MOE-T2EP50223-0008), Singapore Ministry of Education Tier 3 grant “Quantum Geometric Advantage” AcRF Tier 3 (MOE-MOET32023-0003) and A*STAR MTC Programmatic Grant M23M2b0056. Z.L. thanks prof. Yidong Chong for insightful discussions on the theory of amorphous structures. K.S.N. acknowledges support from Singapore National Research Foundation (Research Centre of Excellence award to the Institute for Functional Intelligent Materials, I-FIM, project No. EDUNC-33-18-279-V12), the Royal Society (UK, grant number RSRP\R\190000). Z.W. acknowledges funding support from A*STAR MTC YIRG grant M23M7c0122. X.L.W. and B.T. acknowledge the support from National Research Foundation, Singapore and IMDA (FCP R&D FCP-CNRS-RG-2022-022) and Singapore Ministry of Education (MOE Tier 2 MOE-T2EP50121-0001). Z.H. and Z.Z. acknowledge supports from National Key Research and Development Program of China (2024YFA1409600), National Natural Science Foundation of China (12261160367, 12225205, U2441272), and a Project Funded by the Priority Academic Program Development of Jiangsu Higher Education Institutions. X.W.W. acknowledges supports from National Natural Science Foundation of China (Grant No. 62371448) and Suzhou Municipal Bureau of Science & Technology (Grant No. ZXL2023339, SJC2023004). C.Z.⁸ acknowledges supports from National Natural Science Foundation of China (12274067), and Fundamental Research Funds for the Central Universities. Z.C. acknowledges supports from National Natural Science Foundation of China (Grant No. 52402044), and Shenzhen Science and Technology Innovation Commission (JCYJ20240813160206009, KQTD20221101115627004). M.L.P. acknowledges the generous funding provided by the Swiss National Science Foundation under the Eccellenza Professorial Fellowship no. PCEFP2_203663 and the Swiss State Secretariat for Education, Research, and Innovation (SERI) under contract number MB22.00076 and MB23.00422. W.Z. acknowledges support from the Beijing Outstanding Young Scientist Program (BJJWZYJH01201914430039) and the CAS Project for Young Scientists in Basic Research (YSBR-003). The computations were partly performed at the High-Performance Computational Center at NUAU. This research benefited from resources and supports from the Electron Microscopy Center at the University of Chinese Academy of Sciences.

Author contributions

Y.D., Z.W., Z.H. and A.L. contributed equally to this work. Z.L. and Y.D. conceived and supervised the project. Y.D. synthesized the sample, performed XPS, SEM, Raman characterization and did data analysis. X.L.W., M.C., and B.K.T. performed the magnetron sputtering. Z.W. and K.S.N. supervised the electrical transport part. Z.W. designed and carried out the transport measurements and performed the data analysis. Z.C. and J.L. fabricated the vertical tunneling transport devices. K.Y.

fabricated the in-plane transport devices. W.M., J.Y., and X.X.Z.¹ helped transfer the sample. X.W.W., C.Z.¹, R.D., and Q.F. provided suggestions on data analysis and commented on the manuscript. Z.Z. supervised the theoretical part: Z.H. proposed the growth theory and performed the Monte Carlo simulations. P.Z. performed the DFT calculations. J.Z. and M.P. performed the calculations of graphene models. W.Z. supervised the STEM characterization part. A.L., X.Z., Y.W., and X.X.Z.¹⁰ performed the STEM and data analysis. D.Y. and C.Z.⁸ performed the EDX characterization of precursor film. Y.D., Z.W., and Z.H. wrote the manuscript with input from other authors. All the authors discussed and commented on the manuscript.

Competing interests

The authors declare no competing interests.

Additional information

Supplementary information The online version contains supplementary material available at <https://doi.org/10.1038/s41467-025-63872-7>.

Correspondence and requests for materials should be addressed to Wu Zhou, Zhuhua Zhang, Kostya S. Novoselov or Zheng Liu.

Peer review information *Nature Communications* thanks the anonymous reviewer(s) for their contribution to the peer review of this work. A peer review file is available.

Reprints and permissions information is available at <http://www.nature.com/reprints>

Publisher's note Springer Nature remains neutral with regard to jurisdictional claims in published maps and institutional affiliations.

Open Access This article is licensed under a Creative Commons Attribution-NonCommercial-NoDerivatives 4.0 International License, which permits any non-commercial use, sharing, distribution and reproduction in any medium or format, as long as you give appropriate credit to the original author(s) and the source, provide a link to the Creative Commons licence, and indicate if you modified the licensed material. You do not have permission under this licence to share adapted material derived from this article or parts of it. The images or other third party material in this article are included in the article's Creative Commons licence, unless indicated otherwise in a credit line to the material. If material is not included in the article's Creative Commons licence and your intended use is not permitted by statutory regulation or exceeds the permitted use, you will need to obtain permission directly from the copyright holder. To view a copy of this licence, visit <http://creativecommons.org/licenses/by-nc-nd/4.0/>.

© The Author(s) 2025

¹School of Materials Science & Engineering, Nanyang Technological University, Singapore, Singapore. ²Institute for Functional Intelligent Materials, National University of Singapore, Singapore, Singapore. ³State Key Laboratory of Mechanics and Control for Aerospace Structures, Key Laboratory for Intelligent Nano Materials and Devices of Ministry of Education and Institute for Frontier Science, Nanjing University of Aeronautics and Astronautics, Nanjing, China. ⁴School of Physical Sciences, University of Chinese Academy of Sciences, Beijing, China. ⁵Guangdong Provincial Key Laboratory of Nano-Micro Materials Research, School of Advanced Materials, Peking University Shenzhen Graduate School, Peking University, Shenzhen, China. ⁶IRL 3288 CINTRA (CNRS-NTU-THALES), Nanyang Technological University, Singapore, Singapore. ⁷School of Electrical and Electronic Engineering, Nanyang Technological University, Singapore, Singapore. ⁸SEU-FEI Nano-Pico Center, Key Laboratory of MEMS of Ministry of Education, School of Integrated Circuits, Southeast University, Nanjing, China. ⁹i-Lab, Institute of NanoTech and Nano-Bionics, Chinese Academy of Sciences, Suzhou, China. ¹⁰School of Materials Science and Engineering, Peking University, Beijing, China. ¹¹Nanofabrication Laboratory, National Center for Nanoscience and Technology, Technology, University of Chinese Academy of Sciences, Beijing, China. ¹²Transport at Nanoscale Interfaces Laboratory, Empa, Swiss Federal Laboratories for Materials Science and Technology, Dübendorf, Switzerland. ¹³Department of Information Technology and Electrical Engineering, ETH Zurich, Zurich, Switzerland. ¹⁴Quantum Center, ETH Zürich, Zürich, Switzerland. ¹⁵These authors contributed equally: Ya Deng, Zihao Wang, Zhili Hu, Ang Li. ✉ e-mail: wuzhou@ucas.ac.cn; chuwazhang@nuaa.edu.cn; kostya@nus.edu.sg; z.liu@ntu.edu.sg